

Modeling Buffer Layer IGBT's for Circuit Simulation

Allen R. Hefner, Jr., *Senior Member, IEEE*

Abstract—The dynamic behavior of commercially available buffer layer IGBT's is described. It is shown that buffer layer IGBT's become much faster at high voltages than nonbuffer layer IGBT's with similar low voltage characteristics. Because the fall times specified in manufacturers' data sheets do not reflect the voltage dependence of switching speed, a new method of selecting devices for different circuit applications is suggested. A buffer layer IGBT model is developed and implemented into the Saber circuit simulator, and a procedure is developed to extract the model parameters for buffer layer IGBT's. It is shown that the new buffer layer IGBT model can be used to describe the dynamic behavior and power dissipation of buffer layer IGBT's in user-defined application circuits. The results of the buffer layer IGBT model are verified using commercially available IGBT's.

NOMENCLATURE

A	Device active area (cm ²).
A_{ds}	Body region area (cm ²).
A_{gd}	Gate-drain overlap area (cm ²).
b	μ_n/μ_p Ambipolar mobility ratio.
BV_{cbo}	Collector-base junction breakdown voltage (V).
BV_f	Breakdown voltage nonplanar junction factor.
BV_n	Avalanche multiplication exponent.
BV_k	Temperature-dependent BV_{cbo} coefficients.
B-IGBT	Buffer layer IGBT.
C_{bcj}	Base-collector depletion capacitance (F).
C_{cer}	Collector-emitter redistribution capacitance (F).
C_{dsj}	Drain-source depletion capacitance (F).
C_{gd}	Gate-drain capacitance (F).
C_{gdj}	Gate-drain overlap depletion capacitance (F).
C_{gs}	Gate-source capacitance (F).
C_{oxd}	Gate-drain overlap oxide capacitance (F).
D	Ambipolar diffusivity (cm ² /s).

Manuscript received November 1, 1993; revised October 13, 1994. This paper was presented at the IEEE Power Electronic Specialists Conference June 21, 1993. Contribution of the National Institute of Standards and Technology; not subject to copyright. Certain commercial products are identified in this paper in order to specify the experimental procedure adequately. Such identification does not imply recommendation or endorsement by the National Institute of Standards and Technology, nor does it imply that these products are the best available products for the purpose.

The author is with the Semiconductor Electronics Division, National Institute of Standards and Technology, U.S. Department of Commerce, Technology Administration, Gaithersburg, MD 20899 USA.

IEEE Log Number 9408500.

D_c	Carrier-carrier scattering diffusivity (cm ² /s).
D_{pH}	Hole diffusivity in the HDB (cm ² /s).
D_{pL}	Hole diffusivity in the LDB (cm ² /s).
E_0	Peak electric field (V/cm).
E_{sw}	Turn-off switching energy (J).
HDB	High-doped base region (buffer layer).
I_{bss}	Charge control base current (A).
I_c	Collector current (A).
I_{css}	Charge control collector current (A).
I_{gen}	Thermally generated current (A).
I_K^T	Knee current for current decay rate (A).
$I_{K,L}$	Knee current for $\beta_{tr,L}$ (A).
I_{mos}	MOSFET channel current (A).
I_{mult}	Multiplication current (A).
$I_n(W)$	Electron current at collector end of the LDB (A).
$I_{nH}(x^* = 0)$	Electron current injected into the emitter (A).
I_{pH}	HDB hole current (A).
I_{sne}	Emitter electron saturation current (A).
I_{sne}'	Lumped model parameter for I_{sne} .
I_T	Anode current (A).
K_p	MOSFET transconductance parameter (A/V ²).
K_f	Triode region MOSFET transconductance factor.
k	Boltzmann's constant (J/K).
L	Ambipolar diffusion length (cm).
LDB	Low-doped base region.
M	Avalanche multiplication factor.
NB-IGBT	Nonbuffer layer IGBT.
N_L	Dopant density in LDB (cm ⁻³).
N_H	Dopant density in HDB (cm ⁻³).
n_i	Intrinsic carrier concentration (cm ⁻³).
N_{scl}	Collector-base space charge concentration (cm ⁻³).
N_{sat}	Velocity saturation component of N_{scl} (cm ⁻³).
n_{eff}	Effective LDB dopant density (cm ⁻³).
δp	Excess carrier concentration (cm ⁻³).
$\overline{\delta p}$	Average carrier concentration in LDB (cm ⁻³).
δp_{LO}	δp at HDB edge of the LDB (cm ⁻³).
δp_{HO}	δp at emitter edge of the HDB (cm ⁻³).
δp_{HW}	δp at LDB edge of the HDB (cm ⁻³).
Q_T	Total excess carrier base charge (C).

Q_B	Background LDB mobile carrier charge (C).
Q_H	Excess carrier charge in the HDB (C/cm^2).
Q_{H1}	First term in expression for Q_H .
Q_L	Excess carrier charge in the LDB (C/cm^2).
Q'_L	Iteration variable for Q_L .
Q_{bi}	Emitter-HDB junction built-in charge (C).
q	Electronic charge (1.6×10^{-19} C).
R_b	Conductivity-modulated base resistance (Ω).
T_j	Silicon chip surface temperature (K).
T_{sw}	Effective switching time (s).
V_{ae}	Modulated base resistance voltage (V).
V_{bc}	Base-collector voltage (V).
V_{dg}	Drain-gate voltage (V).
V_{ds}	Drain-source voltage (V).
V_{ebq}	Emitter-base capacitor voltage (V).
V_{ebd}, V_{ebj}	Emitter-base diffusion, depletion voltage (V).
V_{gs}	Gate-source voltage (V).
V_T	MOSFET channel threshold voltage (V).
V_{Td}	Gate-drain overlap depletion threshold (V).
v_{nsat}, v_{psat}	Electron, hole saturation velocity (cm/s).
V_{rt}	Buffer layer reach-through voltage (V).
V_{bi}	Built-in potential of emitter-HDB junction (V).
V_{nrt}	Corresponding V_{bc} for NB-IGBT (V).
V_{on}	On-state voltage (V).
V_{clamp}	Clamp voltage (V).
W	Quasineutral LDB width (cm).
W_L	Metallurgical LDB width (cm).
W_{bcj}	Base-collector depletion width (cm).
W_{dsj}	Drain-source depletion width (cm).
W_{gdj}	Gate-drain overlap depletion width (cm).
W_H	Width of HDB (μm).
W_{nrt}	Corresponding W_{bcj} for NB-IGBT (cm).
W_{eff}	Effective width for base transport (cm).
x, x^*	Position in LDB, HDB (cm).
$\beta_{tr,L}$	Relative tail size for clamped inductive load.
$\beta_{tr,L}^{max}$	Extrapolated zero current value of $\beta_{tr,L}$.
γ	High-level injection condition factor.
ϵ_{si}	Dielectric constant of silicon (F/cm).
θ	Transverse field transconductance factor (1/V).
μ_{eff}	Effective ambipolar mobility ($\text{cm}^2/\text{V}\cdot\text{s}$).
μ_n, μ_p	Electron, hole mobility in LDB ($\text{cm}^2/\text{V}\cdot\text{s}$).
μ_{nc}, μ_{pc}	Carrier-carrier scattering mobilities ($\text{cm}^2/\text{V}\cdot\text{s}$).
μ_{pI}	Ionized impurity scattering component of μ_{pH} .
μ_{pL}	Lattice scattering component of μ_{pH} .
μ_{pH}	HDB mobility ($\text{cm}^2/\text{V}\cdot\text{s}$).
τ_{Ab}	Ambipolar LDB base transit time (μs).
τ_{eff}	Effective excess carrier decay time constant (μs).
τ_{Hb}	HDB base transit time (μs).
τ_H	Excess carrier lifetime in HDB (μs).
τ'_H	Lumped model parameter for τ_H .

τ_L	High-level injection lifetime in LDB (μs).
τ_r	Moving boundary redistribution time (μs).

I. INTRODUCTION

THE Insulated Gate Bipolar Transistor (IGBT) is rapidly becoming the preferred switching device in many power electronic applications. Various IGBT types are available from several power semiconductor device manufacturers utilizing different structures and different structural parameters to optimize the critical device performance trade-offs. In general, the methods used to produce low switching energy losses also result in higher on-state energy losses. As a consequence, many IGBT manufacturers produce several families of IGBT's with different on-state voltage versus switching speed trade-offs. However, each of the different methods used to reduce switching energy produces a different dependence of switching energy on the circuit operating conditions. Therefore, it is also important to consider the method used to reduce the switching energy when selecting an IGBT type for a given circuit application.

The primary methods used to reduce IGBT switching energy are 1) reducing the lifetime of the base region, 2) reducing the injection efficiency of the emitter-base junction, and 3) inclusion of a high-doped buffer layer at the emitter edge of the base. The inclusion of buffer layers in IGBT's has been suggested since the IGBT was first introduced [1], [2]. Fig. 1 is a diagram of the IGBT structure indicating the position of the high-doped buffer layer in the IGBT bipolar transistor base. For the purposes of this paper, IGBT's that contain buffer layers are referred to as buffer layer IGBT's (B-IGBT's) and those that do not contain buffer layers are referred to as nonbuffer layer IGBT's (NB-IGBT's). In addition, the low-doped portion of the IGBT bipolar transistor base is referred to as the low-doped base (LDB) and the buffer layer is referred to as the high-doped base (HDB).

The benefits of the HDB were originally suggested to be 1) an increase in breakdown voltage for a given LDB width, and 2) a faster switching speed due to the reduced bipolar transistor current gain. In general, a lower bipolar transistor current gain results in less stored charge and a faster charge decay rate, and thus reduces the size and decay time of the IGBT turn-off current tail [3]. The HDB reduces the bipolar transistor current gain because the increased background base charge of the high-doped region reduces the emitter injection efficiency, and because the reduced lifetime in the HDB decreases the base transport factor (lifetime generally decreases with increased dopant density).

It was also predicted theoretically in [4] that the buffer layer inclusion method of reducing the bipolar transistor current gain could be used to produce a better trade-off between on-state voltage and switching energy than the conventional lifetime reduction method. The enhanced trade-off occurs because the HDB forms a larger portion of the quasineutral base width at high voltages where a large portion of the LDB is depleted, than at low voltages where the LDB is not depleted. Thus, the HDB reduces the bipolar transistor current gain more during high-voltage switching conditions than during low-voltage on-

state condition. However, the advantages of the B-IGBT's over conventional lifetime reduction IGBT's are only evident for high-voltage switching conditions.

Recently, B-IGBT's (referred to as second generation or ultra fast IGBT's) have become available from several power device manufacturers utilizing the benefits of the HDB described in [4]. The dynamic behavior of these devices is substantially different from NB-IGBT's. For example, a given B-IGBT may behave similarly to a given NB-IGBT for low-voltage on-state conditions and for low-voltage switching conditions, but at high voltages, the current decay rate of the B-IGBT may become much faster than the NB-IGBT. Because IGBT data sheets typically do not specify the voltage dependence of switching energy, it is difficult for circuit designers to determine the most suitable device for a given application from this data book information alone.

The purpose of this paper is to describe the differences in switching behavior between B-IGBT's and NB-IGBT's, and to develop a physics-based B-IGBT model that is suitable for general external circuit operating conditions. The new B-IGBT model is implemented into the Saber¹ circuit simulator and a model parameter extraction sequence is developed for B-IGBT's. Using the model, power electronic circuit designers can examine the advantages and disadvantages of B-IGBT's for different applications. Because the model is based upon structural and material parameters, the model can also be used to develop IGBT structures that are optimized for specific external circuit operating conditions. In addition, the general theory for B-IGBT operation developed in [4] is experimentally verified in this paper for the first time.

II. BUFFER LAYER IGBT MODEL DEVELOPMENT

In [5], [6], an NB-IGBT model was developed that is applicable for general external circuit operating conditions and IGBT's that have been optimized using lifetime reduction or emitter efficiency reduction (methods 1 and 2 above). Although the basic theory for the B-IGBT was developed in [4], the previous analysis assumed a specific simplified circuit operating condition to compare different device types. In this section, a general-purpose circuit simulator model is developed for B-IGBT's (i.e., devices that are optimized using method 3 above). The new B-IGBT model developed in this section combines the nonquasi-static ambipolar transport equations in the LDB [3], [7] with the low-level injection transport equations in the HDB and emitter regions [4]. The boundary conditions at the interfaces between the emitter, HDB, and LDB regions are used to formulate the model in terms of the instantaneous values of the anode current, the total base charge, and the terminal voltages.

A. Boundary Conditions

The coordinate system used to develop the B-IGBT model is shown in Fig. 2, and the symbols used by the model are defined in the nomenclature at the beginning of the paper. In general, the symbols with subscript *H* represent quantities

¹ SaberTM and MAST[®] are trademarks of Analogly Inc., Beaverton, OR.

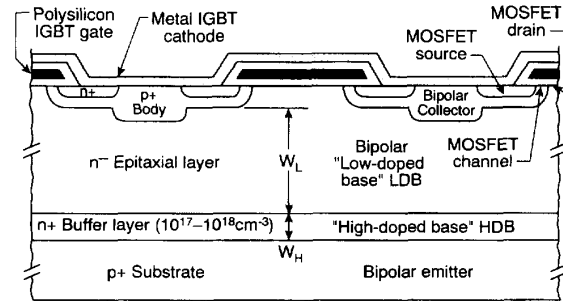


Fig. 1. Schematic of buffer layer IGBT indicating the position of the buffer layer in the IGBT bipolar transistor base.

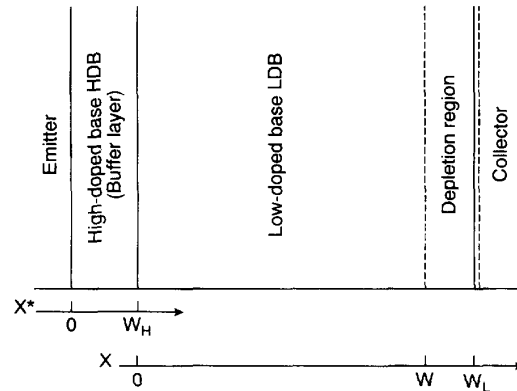


Fig. 2. The coordinate system used to develop the B-IGBT model.

in the HDB, and the symbols with subscript *L* represent quantities in the LDB. The excess carrier concentration at the HDB edge of the quasineutral LDB is defined as:

$$\delta p(x=0) \equiv P_{L0}, \quad (1)$$

and the excess carrier concentrations at the quasineutral edges of the HDB are defined as

$$\delta p(x^*=0) \equiv P_{H0} \quad (2)$$

$$\delta p(x^*=W_H) \equiv P_{HW}, \quad (3)$$

where $x=0$ corresponds to the HDB edge of the quasineutral LDB, and $x^*=0$ corresponds to the emitter edge of the quasineutral HDB. The quantities defined in (1)–(3) are used throughout the development of the B-IGBT model.

The excess carrier concentration at the collector edge of the neutral base ($x=W$) is equal to zero because the collector-base junction is reverse biased for a forward-biased IGBT anode voltage:

$$\delta p(x=W) = 0. \quad (4)$$

The width of the neutral base region depends upon the base-collector voltage:

$$W = W_L - W_{bcj} \quad \text{for } W \geq 0 \quad (5a)$$

where

$$W_{bcj} = \sqrt{2\epsilon_{si}(V_{bc} + 0.6)/qN_L} \quad \text{for } W_{bcj} \leq W_L \quad (5b)$$

because the collector-base depletion region extends into the LDB. However, the width of collector-base depletion region is limited in (5b) to $W_{bcj} \leq W_L$ because the depletion region does not extend significantly into the high-doped HDB. Because the base width depends upon V_{bc} which changes with time during transient conditions, the moving base width boundary condition must be included in the development of the B-IGBT model where the base width boundary velocity is given by

$$\frac{dW}{dt} = \frac{-C_{bcj}}{qN_L A} \cdot \frac{dV_{bc}}{dt} \quad \text{for } W \geq 0. \quad (6)$$

Equation 6 is obtained by differentiating (5) where $C_{bcj} \equiv A\epsilon_{si}/W_{bcj}$ has been used.

The boundary condition for the excess carrier concentration across the HDB-LDB junction is obtained using the quasiequilibrium approximation for the low-level injection conditions in the HDB:

$$P_{HW} = \frac{P_{L0}(P_{L0} + N_L)}{N_H} \approx \frac{P_{L0}^2}{N_H} \quad (7)$$

where the approximate form assumes high-level injection in the LDB. The boundary condition at the emitter-HDB junction is used to relate the electron current injected into the emitter to the excess carrier concentration at the emitter edge of the HDB:

$$I_{nH}(x^* = 0) = I_{sne} \frac{P_{H0}N_H}{n_i^2}. \quad (8)$$

This relationship is developed using the quasiequilibrium condition to relate the carrier concentrations across the emitter-base junction for the low-level injection condition in the HDB, where I_{sne} represents the properties of the emitter determined from the diffusion equation for electrons in the emitter.

B. Collector Current

It is shown in [7] that the quasistatic approximation is not valid for the low-gain, high-level injection conditions that occur in the IGBT. This occurs because the transport of electrons and holes are coupled, and because the neutral base width changes faster (through (6)) than the base transit speed for excess carriers. Using a nonquasi-static approach, the collector current for the thick LDB was shown to be given by [3], [7]

$$I_c = \frac{\gamma I_T}{1+b} + \frac{Q_L}{\tau_{Ab}} + \frac{Q_L}{\tau_r} \quad (9)$$

where the quantities

$$\tau_{Ab} \equiv W^2/2D \quad (10)$$

$$\tau_r \equiv 3Q_B / \left(C_{bcj} \cdot \frac{dV_{bc}}{dt} \right) \quad (11)$$

have been defined here to simplify the mathematical development. The excess carrier charge in the LDB is given in terms of P_{L0} by [3], [7]

$$Q_L = qAWP_{L0}/2. \quad (12)$$

Because the HDB remains in the low-level injection condition for practical use conditions, the transport of holes in the HDB is dominated by diffusion and the transport of electrons and holes are not coupled as in the LDB. The hole current in the HDB is given by [4]

$$I_{pH} = \frac{qAD_{pH}}{W_H} (P_{H0} - P_{HW}) \quad (13a)$$

$$= \frac{Q_H}{\tau_{Hb}} - \frac{2}{\tau_{Hb}} \cdot \frac{W_H}{W_L} \cdot \frac{P_{L0}}{N_H} \cdot Q_L \quad (13b)$$

$$= \frac{Q_H}{\tau_{Hb}} - \frac{4}{\tau_{Hb}} \cdot \frac{W_H}{W_L} \cdot \frac{N_L}{N_H} \cdot \frac{Q_L^2}{Q_B} \quad (13c)$$

where

$$\tau_{Hb} \equiv W_H^2/2D_{pH} \quad (14)$$

has also been defined to simplify the mathematical development. The expression for the excess carrier charge in the HDB [4]:

$$Q_H = \frac{qAW_H}{2} (P_{H0} - P_{HW}) \quad (15)$$

and (12) have also been used to obtain (13b) and (13c).

The total excess carrier charge in the bipolar transistor base is given by the sum of the excess carrier charge in the HDB and in the LDB regions

$$Q_T = Q_L + Q_H. \quad (16)$$

Equating the hole current in the HDB (13b) to the collector current (9) results in an expression for the charge in the LDB in terms of the total base charge and anode current

$$Q_L = \left[Q_T - \left(\frac{\gamma I_T}{1+b} \right) \tau_{Hb} \right] / \left[1 + \frac{\tau_{Hb}}{\tau_{Ab}} + \frac{\tau_{Hb}}{\tau_r} \right] \quad (17)$$

where (16) has been used and the approximation has been made that $P_{L0} \ll N_H$. This approximation follows from (7) for the low-level injection condition in the HDB $P_{HW} \ll N_H$ and is analogous to the approximate form of (32) in [4]. The condition that $I_{pH} \approx I_c$ neglects the influence of recombination in the base on the ratio of the HDB charge to the LDB charge.

Finally, substituting (17) into (9) yields the expression for the B-IGBT collector current

$$I_c = \left[\frac{\gamma I_T}{1+b} + \frac{Q_T}{\tau_{Ab}} + \frac{Q_T}{\tau_r} \right] / \left[1 + \frac{\tau_{Hb}}{\tau_{Ab}} + \frac{\tau_{Hb}}{\tau_r} \right] \quad (18)$$

in terms of Q_T , V_{bc} (through τ_{Ab} and W), and the time rate-of-change of V_{bc} (through τ_r). This expression is similar to the NB-IGBT collector current expression [7] except for the factor in the brackets in the denominator of (18). For $W_H = 0$ (i.e., no HDB), the denominator in (18) is equal to unity and the B-IGBT model reduces to the NB-IGBT model.

C. Charge Decay Rate

The excess majority carrier charge in the bipolar transistor base (equal to the excess minority carrier charge to maintain quasineutrality) is supplied by the electron current that enters the collector end of the base (base current), and decays by recombination in the HDB, recombination in the LDB, and injection of electrons into the emitter

$$\frac{dQ_T}{dt} = I_n(W) - I_{bss} \quad (19)$$

where

$$I_{bss} \equiv \frac{Q_L}{\tau_L} + \frac{Q_H}{\tau_H} + I_{snc} \frac{P_{H0} N_H}{n_i^2}. \quad (20)$$

In the following, expressions are developed for Q_H and P_{H0} that are used with (17) for Q_L to evaluate the charge decay rate in terms of Q_T and I_T .

Solving (13c) for Q_H yields

$$Q_H = Q_{H1} + 4 \cdot \frac{W_H}{W_L} \cdot \frac{N_L}{N_H} \cdot \frac{Q_L^2}{Q_B}, \quad (21)$$

where

$$Q_{H1} = \frac{\left[Q_T \left(\frac{\tau_{Hb}}{\tau_{Ab}} + \frac{\tau_{Hb}}{\tau_r} \right) + \frac{\gamma I_T}{1+b} \tau_{Hb} \right]}{\left[1 + \frac{\tau_{Hb}}{\tau_{Ab}} + \frac{\tau_{Hb}}{\tau_r} \right]} \quad (22)$$

is obtained using (18) to evaluate $Q_{H1} \equiv I_c \cdot \tau_{Hb}$. Although the second term in (13b) is negligible in developing the expression for the LDB charge (17) and the collector current (18), it is important to include this term (second term in (21)) in calculating the charge decay rate of (19) and (20) because the lifetime in the HDB is much smaller than that in the LDB.

Solving (13a) for P_{H0} yields

$$P_{H0} = \frac{W_H I_{pH}}{q A D_{pH}} + P_{HW} \quad (23a)$$

$$= \frac{W_H}{q A D_{pH}} \cdot \frac{Q_{H1}}{\tau_{Hb}} + \frac{P_{L0}(P_{L0} + N_L)}{N_H} \quad (23b)$$

$$= \frac{W_H}{q A D_{pH}} \cdot \frac{Q_{H1}}{\tau_{Hb}} + \left(\frac{2}{q A W} \right)^2 \cdot \frac{Q_L^2}{N_H} \quad (23c)$$

where (7), (18), and (22) have been used to obtain (23b) and (12) has been used to obtain (23c).

Finally, substituting (21) and (23c) into (20) yields

$$I_{bss} = \frac{Q_L}{\tau_L} + \frac{Q_{H1}}{\tau_H} + 4 I'_{snc} \frac{N_L}{n_i^2} \frac{Q_L^2}{Q_B^2} \quad (24)$$

where

$$\frac{1}{\tau'_H} \equiv \frac{1}{\tau_H} + \frac{2 N_H I_{snc}}{q A W_H n_i^2} \quad (25)$$

$$I'_{snc} \equiv I_{snc} + \frac{n_i^2 q A W_H}{\tau_H N_H}. \quad (26)$$

Thus, using (17), (19), (22), and (24), the charge decay rate is expressed in terms of the total base charge and the total

current. It is shown in the parameter extraction section below that the quantities τ_L , τ'_H , and I'_{snc} are readily extracted from the terminal electrical characteristics of the IGBT. The values of τ'_H and I'_{snc} can also be calculated from the physical and structural parameters on the right-hand side of (25) and (26).

D. Emitter-Base Voltage

The emitter-base voltage for the B-IGBT was analyzed in [4]. Because the emitter-base voltage is a small component of the IGBT anode voltage for high-voltage transient conditions, but is a significant component for the low-voltage on-state conditions, the emitter-base voltage expression is developed using the steady-state carrier distribution. However, the expressions are formulated in terms of the instantaneous base charge determined by the dynamic model, so that the model also describes the dynamic saturation effect. The procedure used to describe the B-IGBT emitter-base voltage is similar to that used for the general purpose NB-IGBT model [6].

The IGBT emitter-base voltage can be written as

$$V_{eb} = V_{ebq} + R_b, \quad (27)$$

where for forward conduction, V_{ebq} is equal to the emitter-base diffusion capacitance voltage V_{ebd} , and for reverse blocking, V_{ebq} is equal to the emitter-base depletion capacitance voltage V_{ebj} . For forward conduction, (21), (25), and (27) of [4] can be combined to obtain the expressions for the emitter-base diffusion capacitance voltage

$$V_{ebd} = \frac{k T_j}{q} \ln \left(\frac{P_{H0} N_H}{n_i^2} + 1 \right) - \frac{D}{\mu_n} \ln \left(\frac{P_{L0} + N_L}{N_L} \right) \quad (28)$$

and the conductivity modulated base resistance

$$R_b = W / (q \mu_{eff} A n_{eff}), \quad (29)$$

where the expression for n_{eff} in terms of P_{L0} is given in [4]. The steady-state relationship between P_{L0} and Q_L :

$$P_{L0} = Q_L / \left(q A L \tanh \frac{W}{2L} \right) \quad (30)$$

is used for the emitter-base voltage expressions so that the model accurately describes the steady-state on-state voltage. The value of P_{H0} used in (28) is obtained from (23b) in terms of Q_{H1} and P_{L0} .

For reverse blocking conditions and for small emitter-base voltage conditions, the emitter-base voltage is determined by the emitter-base depletion capacitance charge. In the model, the emitter-base depletion capacitance charge is represented using the same system variable Q_T used to represent the emitter-base diffusion capacitance charge. For the depletion-capacitance-dominated case, the emitter-base capacitor voltage is given by

$$V_{ebj} = V_{bi} - (Q_T - Q_{bi})^2 / (2q N_H \epsilon_{si} A^2) \quad (31)$$

where

$$Q_{bi} = A \sqrt{2 \epsilon_{si} q N_H V_{bi}} \quad (32)$$

and the built-in potential of the emitter-HDB junction V_{bi} is approximately equal to 1.0 V. For the B-IGBT, the emitter-base depletion capacitor expressions depend upon the HDB dopant density, whereas for the NB-IGBT, they depend upon the LDB dopant density. In the model, a continuous transition between the depletion capacitance and the diffusion capacitance for small forward-biased emitter-base voltages is obtained by using the larger of the two capacitances or equivalently the minimum of the capacitor voltages [6].

E. Avalanche Multiplication

The carrier multiplication factor is important in determining the avalanche breakdown voltage, the leakage current, and the dynamic avalanche-sustaining voltage. In the NB-IGBT model, the empirical expressions for carrier multiplication factor are used

$$M = 1/[1 - (V_{nrt}/BV_{cbo})^{BV_n}] \quad (33)$$

$$BV_{cbo} = BV_f \cdot 5.34 \times 10^{13} \cdot N_L^{-0.75} \quad (34)$$

which are functions of the LDB dopant density and the collector-base voltage (represented here by V_{nrt}). These same formula are also used for the B-IGBT model, but with an effective value of V_{nrt} calculated in terms of V_{bc} as described below.

Equations (33) and (34) are based upon a one-sided step junction where the depletion region extends into a region with constant dopant density. For this case the electric field distribution is triangular as shown in Fig. 3(a), and the base-collector voltage can be expressed in terms of peak electric field E_0 as

$$V_{nrt} = E_0 W_{nrt}/2 \quad (35a)$$

where

$$W_{nrt} = \sqrt{2\epsilon_{si}(V_{nrt} + 0.6)/qN_L} \quad (35b)$$

is the depletion width for the case where the depletion region extends into a region with constant dopant density and does not reach through to an HDB region.

For typical B-IGBT's, the depletion region reaches through to the HDB before avalanche breakdown occurs. The reach-through voltage is given by

$$V_{rt} = (qW_L^2 N_L / 2\epsilon_{si}) - 0.6 \quad (36)$$

For voltages larger than the reach-through voltage, the electric field distribution becomes trapezoidal as shown in Fig. 3(b) because the depletion region does not extend significantly into the high-doped HDB. For the trapezoidal distribution, the collector-base voltage can be expressed in terms of the peak electric field as

$$V_{bc} = E_0 \left(1 - \frac{W_{bcj}}{2W_{nrt}} \right) W_{bcj} \quad (37)$$

where W_{bcj} is given by (5b) which is limited by $W_{bcj} \leq W_L$, and W_{nrt} is defined by (35b) with V_{nrt} replaced by V_{bc} .

Because the avalanche multiplication coefficients depend exponentially upon the magnitude of the electric field, the

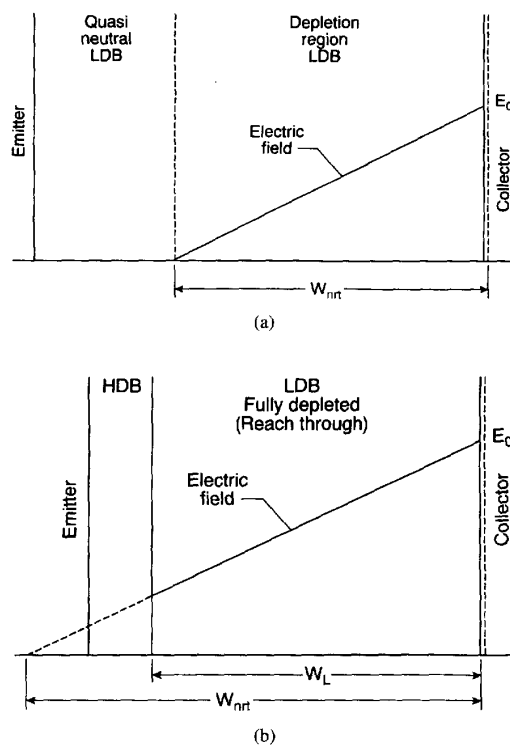


Fig. 3. Electric field distribution for a) one-sided step junction of NB-IGBT and b) trapezoidal distribution of B-IGBT for reach-through condition.

multiplication factor M is primarily determined by the peak electric field E_0 . Therefore, an expression for the multiplication factor M for the B-IGBT is obtained by expressing the base-collector voltage for the NB-IGBT in terms of the B-IGBT base-collector voltage with the same peak electric field. To do this, E_0 is eliminated between (35a) and (37) to obtain

$$V_{nrt} = \frac{V_{bc}}{\frac{W_{bcj}}{W_{nrt}} \left(2 - \frac{W_{bcj}}{W_{nrt}} \right)} \quad (38)$$

where W_{bcj} is given by (5b) and W_{nrt} is given by (35b) with V_{nrt} replaced by V_{bc} . For $V_{bc} < V_{rt}$, $W_{nrt} = W_{bcj}$ and the multiplication factor reduces to the expression for the NB-IGBT.

III. SABER SIMULATOR IMPLEMENTATION

The previously developed NB-IGBT model has been implemented into several circuit and system simulation programs [8]–[10]. The NB-IGBT model has also been extended to include dynamic electro-thermal effects [11] so that the model can be used in conjunction with the thermal component models for various packages and heat sinks to simulate the electro-thermal behavior of electronic circuits and systems [12], [13]. Due to the ease of implementing new models into the Saber simulator using the MAST modeling language (an analog-hardware-description-language AHDL), the Saber simulator is used in this work. The B-IGBT model is implemented into the Saber simulator similarly to the NB-IGBT model described in

[9], and the electro-thermal effects are implemented similarly to those described in [11].

A. Model Formulation

To implement the IGBT model presented in Section I into the Saber simulator, the model is formulated such that the components of current flow into each electrical node and the components of heat flow into the thermal node are expressed in terms of the nonlinear functions of the system variables listed in Table I and in terms of the time rate-of-change of these functions of the system variables. The system variables are the voltages at the electrical nodes, the temperature at the thermal node, and the system variables defined to evaluate implicit model functions. The components of current flow between electrical nodes of the B-IGBT model are the same as those for the NB-IGBT model indicated in Fig. 6 of [9] and the components of heat flow into the thermal node are the same as those for the electro-thermal NB-IGBT model described in Fig. 4(b) of [11]. However, the model equations used to describe each of the components of current are different for the B-IGBT model.

The functions of the system variables for the B-IGBT model (Table I) are similar to those for the NB-IGBT model (Table I of [9]) except that the expressions developed in Section I for the B-IGBT currents, excess carrier charges, emitter-base voltage, and carrier multiplication factor are used. In addition, the depletion width and depletion region charges are changed from the expressions in [9] to account for the case when the collector-base depletion region reaches through to the HDB. The system variables introduced to account for implicit model equations are also the same as those for the NB-IGBT model except for the addition of the system variable Q'_L . This variable is required because the expression for Q_L in Table I depends upon the values of γ and I_T which are evaluated using the value of Q'_L . The model could also be implemented without the additional system variable by using the steady-state relationship between Q_L and Q_T to approximately evaluate γ and the emitter-base voltage expressions.

B. Electro-Thermal Model

In the electro-thermal network simulation methodology introduced in [12], the electro-thermal semiconductor devices have a thermal terminal that is connected to the thermal network component models for the silicon chip, packages, and heat sinks [13]. To include the electro-thermal effects in the B-IGBT model: 1) The functions in Table I are expressed in terms of the instantaneous temperature at the IGBT thermal terminal (T_j) using the temperature-dependent B-IGBT model parameters and the temperature-dependent physical properties of silicon. 2) The components of heat flow into the thermal terminal are expressed in terms of the internal voltages and current. The internal currents and voltages are used to calculate the power dissipation, because a portion of the power that enters the electrical terminals is stored as electric field energy in the internal capacitors and is not dissipated as heat.

The temperature-dependent B-IGBT model parameters are similar to those for the NB-IGBT (Table II of [11]), except for

the addition of an expression for the temperature-dependent HDB lifetime. The temperature-dependent physical properties of silicon are also similar to those for the NB-IGBT (Table I of [11]) except that the temperature dependence of the HDB mobility is different from that of the LDB mobility. This occurs because the temperature dependence of the ionized impurity scattering component of mobility [14]:

$$\mu_{pI}(T_j) = 45 \cdot [1 + (1.2 \times 10^{18}/N_H) \cdot (T_j/300)] \quad (39)$$

is different than the temperature dependence of the lattice scattering component of mobility:

$$\mu_{pL}(T_j) = 450 \cdot (300/T_j)^{2.5}. \quad (40)$$

The hole mobility in the HDB is given by

$$\mu_{pH}(T_j) = 1/(1/\mu_{pI} + 1/\mu_{pL}). \quad (41)$$

The ionized impurity scattering component of mobility is not important in the LDB at room temperature due to the low dopant density. For example, the hole mobility in the LDB decreases to one-half of its value with a temperature increase from 300 K to 400 K, whereas the mobility of the HDB with $N_H = 2.4 \times 10^{17} \text{ cm}^{-3}$ only decreases by 20%.

C. Numerical Convergence

In the Saber template for the B-IGBT model, the equations in Table I are formulated so that they are continuous and nonsingular in the range that the system variables may take during the iterations required to solve the system of nonlinear model equations. For example, the expression for C_{cer} in Table I must be reformulated because it has the value of W in the denominator (through Q_B) and W becomes equal to zero when the collector-base depletion region reaches through to the buffer layer. To prevent numerical overflows in the calculation of C_{cer} , the value of Q_L/W is calculated directly using an expression that does not result in division by W (i.e., the expression for Q_L in Table I with W^2 replaced by W). The value of W used in the hyperbolic functions must also be bounded for W near zero, and the value of W_{eff} must be bounded for large negative values of dV_{bc}/dt . In addition, the values of the base charges are bounded by $0 \leq Q_L < Q_T$ and $Q_H \leq Q_T$.

IV. BUFFER LAYER IGBT PARAMETER EXTRACTION

An extraction sequence was presented in [8], [15] for NB-IGBT's. The extraction sequence can be used to develop IGBT component libraries for circuit simulators. However, the behavior of B-IGBT's is substantially different from NB-IGBT's and the extraction sequence of [8], [15] is not adequate for B-IGBT's. For B-IGBT's, the additional parameters of the HDB must be extracted, and the procedure used to obtain the parameters of the LDB must be modified. Table II lists the parameters of a typical ultra-fast B-IGBT at a temperature of 300 K. The extraction sequence presented in this section can be used to extract the model parameters of B-IGBT's and reduces to the NB-IGBT extraction sequence [8], [15] if the HDB is not present.

TABLE I
FUNCTIONS OF SYSTEM VARIABLES

$N_{sat} = I_c / (qAv_{psat}) - I_{mos} / (qAv_{nsat})$	$P_{L0} = Q'_L / (qAL \tanh \frac{W}{2L})$
$N_{scl} = N_L + N_{sat}$	$P_{H0} = 2Q_H / (qAW_H) + P_{L0}(P_{L0} + N_L) / N_H$
$V_{rt} = qW_L^2 N_{scl} / 2\epsilon_{si} - 0.6$	$\bar{\delta p} \equiv P_{L0} \sinh(W/2L) / \sinh(W/L)$
$W_{gdj} = \sqrt{2\epsilon_{si}(V_{dg} + V_{Td}) / qN_{scl}}$ for $W_{gdj} \leq W_L$	$n_{eff} \equiv \frac{\frac{W}{2L} \sqrt{N_L^2 + P_{L0}^2} \operatorname{csch}^2(\frac{W}{2L})}{\operatorname{arctanh} \left[\frac{\sqrt{N_L^2 + P_{L0}^2} \operatorname{csch}^2(\frac{W}{2L}) \tanh(\frac{W}{2L})}{N_L + P_{L0} \operatorname{csch}(\frac{W}{L}) \tanh(\frac{W}{2L})} \right]}$
$W_{dsj} = \sqrt{2\epsilon_{si}(V_{ds} + 0.6) / qN_{scl}}$ for $W_{dsj} \leq W_L$	$R_b = \begin{cases} W / (q\mu_{nc}AN_L) & \text{for } Q_T < 0 \\ W / (q\mu_{eff}An_{eff}) & \text{for } Q_T \geq 0 \end{cases}$
$W_{bcj} = \sqrt{2\epsilon_{si}(V_{bc} + 0.6) / qN_{scl}}$ for $W_{bcj} \leq W_L$	$V_{ebj} = 1.0 - (Q_T - Q_{bi})^2 / (2qN_H\epsilon_{si}A^2)$
$W_{nrt} = \sqrt{2\epsilon_{si}(V_{bc} + 0.6) / qN_{scl}}$	$V_{ebd} = \frac{kT_j}{q} \ln \left[\frac{P_{H0}N_H}{n_i^2} + 1 \right] - \frac{D_c}{\mu_{nc}} \ln \frac{P_{L0} + N_L}{N_L}$
$W = W_L - W_{bcj}$	$V_{ebq} = \begin{cases} V_{ebj} & \text{for } Q_T < 0 \\ \min(V_{ebj}, V_{ebd}) & \text{for } Q_{bi} > Q_T \geq 0 \\ V_{ebd} & \text{for } Q_T \geq Q_{bi} \end{cases}$
$W_{eff} = \sqrt{W^2 + W_H^2 \frac{D_c}{D_{pH}} + \frac{W_H^2}{2D_{pH}} \cdot \frac{WC_{bcj}}{3qN_LA} \cdot \frac{dV_{bc}}{dt}}$	$V_{nrt} = \frac{V_{bc}}{\frac{W_{bcj}}{W_{nrt}} \left(2 - \frac{W_{bcj}}{W_{nrt}} \right)}$
$\gamma = Q'_L / (Q'_L + Q_B)$	$BV_{cbo} = BV_f \cdot 5.34 \times 10^{13} \cdot N_{scl}^{-0.75}$
$Q_{gs} = C_{gs}V_{gs}$	$M = 1 / [1 - (V_{nrt} / BV_{cbo})^{BV_n}]$
$Q_B = qAWN_{scl}$	$I_T = V_{ae} / R_b$
$Q_{bi} = A\sqrt{2\epsilon_{si}qN_H1.0}$	$I_{css} = \frac{W^2}{W_{eff}^2} \cdot \frac{\gamma I_T}{(1+b)} + \frac{Q_T D_c}{W_{eff}^2}$
$Q_{ds} = \begin{cases} A_{ds} \sqrt{2\epsilon_{si}(V_{ds} + 0.6)qN_{scl}} & \text{for } V_{ds} \leq V_{rt} \\ qA_{ds}W_LN_{scl} + A_{ds}\epsilon_{si}(V_{ds} - V_{rt})/W_L & \text{for } V_{ds} > V_{rt} \end{cases}$	$I_c = I_{css} + C_{cer} \cdot dV_{ec} / dt$
$Q_L = \frac{W^2}{W_{eff}^2} \left(Q_T - \frac{\gamma I_T}{(1+b)} \cdot \frac{W_H^2}{2D_{pH}} \right)$	$I_{bss} = \frac{Q_L}{\tau_L} + \frac{Q_{H1}}{\tau_H} + \frac{Q_B^2}{Q_B^2} \cdot \frac{4N_{scl}^2 I_{sne}'}{n_i^2}$ for $V_{gs} < V_T$
$Q_{H1} = Q_T - Q_L$	$I_{mos} = \begin{cases} 0 & \text{for } V_{gs} < V_T \\ \frac{K_p K_f \left[(V_{gs} - V_T)V_{ds} - \frac{K_f V_{ds}^2}{2} \right]}{[1 + \theta(V_{gs} - V_T)]} & \text{for } V_{ds} \leq \frac{(V_{gs} - V_T)}{K_f} \\ \frac{K_p (V_{gs} - V_T)^2}{2[1 + \theta(V_{gs} - V_T)]} & \text{for } V_{ds} > \frac{(V_{gs} - V_T)}{K_f} \end{cases}$
$C_{bcj} \equiv Ae_{si} / W_{bcj}$	$I_{gen} = qn_i A \sqrt{2\epsilon_{si}V_{bc} / qN_{scl}} / \tau_L$
$C_{dsj} = (A - A_{gd})\epsilon_{si} / W_{dsj}$	$I_{mult} = (M - 1) \cdot (I_{mos} + I_c) + M \cdot I_{gen}$
$C_{gdj} = A_{gd}\epsilon_{si} / W_{gdj}$	
$C_{gd} = \begin{cases} C_{oxd} & \text{for } V_{ds} \leq V_{gs} - V_{Td} \\ C_{oxd}C_{gdj} / (C_{oxd} + C_{gdj}) & \text{for } V_{ds} > V_{gs} - V_{Td} \end{cases}$	
$C_{cer} = \frac{W^2}{W_{eff}^2} \cdot \frac{Q_T}{Q_B} \cdot C_{bcj}$	
$1/\mu_c = (\bar{\delta p} \ln(1 + \alpha_2 (\bar{\delta p})^{-2/3})) / \alpha_1$	
$\mu_{nc} = 1 / (1/\mu_n + 1/\mu_c)$	
$\mu_{pc} = 1 / (1/\mu_p + 1/\mu_c)$	
$\mu_{eff} = \mu_{nc} + \gamma\mu_{pc}$	
$D_c = 2(kT_j/q)\mu_{nc}\mu_{pc} / [\mu_{nc} + \mu_{pc}]$	
$L = \sqrt{D_c \tau_L}$	

A. Current Decay Rate

The current tail decay rate for the clamped inductive load turn-off can be used to extract the parameters τ_L , τ_H' , and I_{sne}' . For the clamped inductive load circuit shown in Fig. 4, the MOSFET channel current is removed rapidly when the gate voltage is switched below the IGBT threshold voltage, so the anode voltage rises to maintain the constant inductor current. After the anode voltage reaches the clamp voltage, the anode voltage remains constant at the clamp supply voltage.

The anode current then drops rapidly due to the removal of the collector-base junction depletion capacitance current, the moving boundary redistribution capacitance current, and the component of hole current associated with the base current for ambipolar transport. After the initial rapid fall in current, the anode current decay rate is determined by recombination in the LDB, recombination in the HDB, and by injection of electron current into the emitter.

Because the anode voltage is constant and the MOSFET current is zero after the anode voltage reaches the clamp

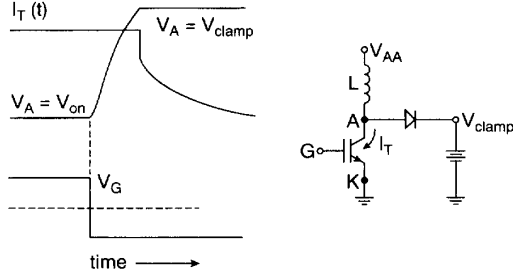


Fig. 4. Clamped inductive load circuit indicating typical IGBT turn-off anode current and anode voltage waveforms.

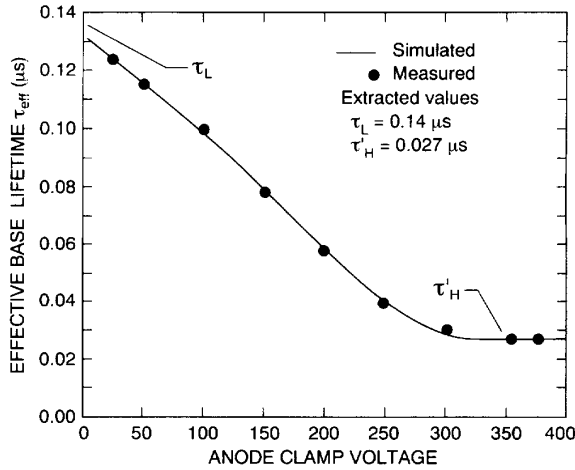


Fig. 5. Comparison of measured values of τ_{eff} versus clamp voltage with model using extracted model parameters.

voltage, $I_c = I_T$ and (17), (18), (19), (22), and (24) can be combined to obtain the extraction equations

$$\frac{d \ln(I_T)}{dt} = -\frac{1}{\tau_{eff}} \left(1 + \frac{I_T}{I_k'} \right) \quad (42)$$

$$\frac{1}{\tau_{eff}} \equiv \left[\frac{W^2}{\tau_L} + \left(\frac{2D_{pL}}{D_{pH}} \right) \frac{W_H^2}{\tau_H'} \right] / \left[W^2 + \left(\frac{2D_{pL}}{D_{pH}} \right) W_H^2 \right] \quad (43)$$

$$\frac{1}{I_k' \tau_{eff}} \equiv \left[\frac{W^2 I_{sne}'}{q^2 n_i^2 A^2 D_{pL}} \right] / \left[W^2 + \left(\frac{2D_{pL}}{D_{pH}} \right) W_H^2 \right] \quad (44)$$

where (10), (14), and the relation $2D_{pL}/D = 1 + 1/b$ have been used. The values of τ_{eff} and I_k' for a given clamp voltage are obtained in the same way as in the previously developed NB-IGBT extraction sequence, i.e., from the slope and zero current intercept of the measured values of $d \ln(I_T)/dt$ versus current (42). However, for the B-IGBT, the effective lifetime defined in (43) is a function of the clamp voltage through (5). Therefore, this extraction procedure must be performed at several clamp voltages for B-IGBT's, whereas for NB-IGBT's the measured value of τ_{eff} is independent of voltage.

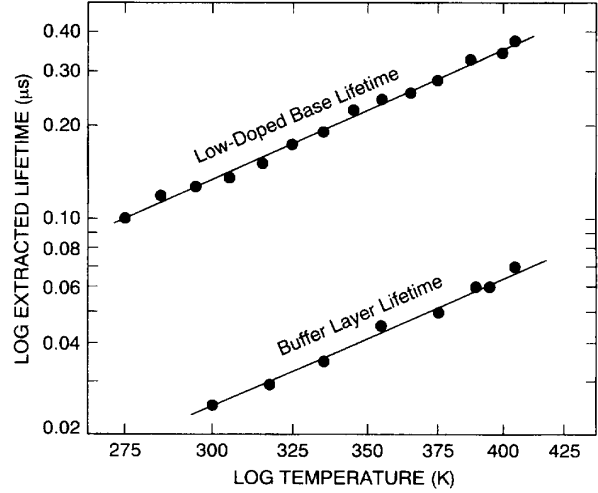


Fig. 6. Extracted values of the HDB and LDB lifetimes versus temperature.

Fig. 5 compares the measured values of τ_{eff} versus clamp voltage with the values calculated using the extracted model parameters in Table II to evaluate (5) and (43). The value of the effective lifetime varies by a factor of five between the low- and high-voltage conditions. Using the measured values of τ_{eff} versus voltage, the values of the HDB and LDB lifetimes can be extracted. The value of the HDB lifetime is readily obtained from the high-voltage value of τ_{eff} in Fig. 5 because the LDB is completely depleted. The value of the LDB lifetime is extracted from the low-voltage values of τ_{eff} in Fig. 5 by solving (5) and (43) for τ_L , using the value of τ_H' obtained as described above and the values for W_L , W_H and N_L obtained as described below. Fig. 6 shows the extracted values of the HDB and LDB lifetimes versus temperature. The slopes of the log of extracted lifetime versus log of temperature are used to obtain the temperature coefficients of τ_H' and τ_L .

B. Current Tail Size

The values of N_L , W_L , and W_H in Table II can be extracted from the relative size of the turn-off current tail for the clamped inductive load turn-off ($\beta_{tr,L}$) or obtained directly from the device structural parameters. Although it is preferable to use the structural parameters, this information is not always available, so a method is described here for extracting these parameters from the terminal electrical characteristics. In [8], [15], a method is described for extracting the base width and dopant density from the relative size of the turn-off current tail for constant anode supply voltage switching. However, for high-speed devices, the current tail is extremely small for constant anode supply voltage switching and the clamped inductive load current tail size is the preferred characteristic for extracting the base widths and dopant densities.

The relative size of the inductive load turn-off current tail can be defined as

$$\frac{1}{\beta_{tr,L}} \equiv \frac{I_T(0^-) - I_T(0^+, V_{on})}{I_T(0^+, V_{clamp})} \quad (45)$$

For NB-IGBT's, this expression can be evaluated to obtain explicit extraction equations for W_L and N_L in terms of the measured values of $\beta_{tr,L}$. Equation (45) can also be evaluated using the B-IGBT model, but the model parameters cannot be expressed independently of one another, and some iteration would be required to determine the model parameters. However, an approximate explicit extraction equation is obtained for the B-IGBT by assuming that the transport equations in the HDB are the same as those in the LDB in calculating the steady-state current (i.e., adding the first term on the right-hand side of (9) to (13b))

$$\frac{1}{\beta_{tr,L}} \approx \frac{1}{\beta_{tr,L}^{max}} \left(1 + \frac{I_T(0^+, V_{clamp})}{I_{K,L}} \right) \quad (46)$$

$$\frac{1}{\beta_{tr,L}^{max}} \approx \frac{W_{eff}'^2}{2D \tau_{eff}(V_{on})} \quad (47)$$

$$W_{eff}' = \sqrt{W^2 + \left(\frac{2D_{pL}}{D_{pH}} \right) \cdot W_H^2} \quad (48)$$

For $W_H = 0$, these extraction equations reduce to those for the NB-IGBT clamped inductive load tail size.

To measure the values of $\beta_{tr,L}$, the initial size of the current tail for the clamp voltage approximately equal to the on-state anode voltage $I_T(0^+, V_{on})$ is subtracted from the steady-state anode current $I_T(0^-)$, and this quantity is then divided by the initial value of the tail current for several clamp voltages $I_T(0^+, V_{clamp})$. The value of $\beta_{tr,L}^{max}$ is obtained by extrapolating the measured values of $1/\beta_{tr,L}$ versus current to the zero current intercept [8], [15]. Equation (47) is then used to calculate W_{eff}' from the measured values of $\beta_{tr,L}^{max}$ where $\tau_{eff}(V_{on})$ is the measured value of τ_{eff} for the clamp voltage approximately equal to the on-state voltage (see Fig. 5). This procedure is performed at several clamp voltages, and the values of N_L , W_L , and W_H are extracted from W_{eff}' versus clamp voltage using (48) and (5).

For devices in which τ_{eff} differs substantially from the lifetime in the LDB, the values of W_L , W_H , and N_L extracted using the approximate (47) can differ substantially from the actual values. This occurs because the first term in (9) reduces the amount of charge in the LDB required to produce a hole current equal to that in the HDB. However, the values of $\sqrt{N_L}$, W_L , and W_H obtained using (47) are larger than the actual values by the same factor. Therefore, these values can be scaled by the same factor to fit the model equations without the approximations of (47). Another difficulty in extracting the base widths using $\beta_{tr,L}$ occurs because the tail current waveforms must be extrapolated back to the time when the charge begins to decay (time when gate voltage is switched below threshold). However, simulations of the extraction circuit can be used to verify the accuracy of the extrapolations.

C. MOSFET and Capacitance Parameters

Although the HDB dopant density N_H influences the effective value of I'_{snc} , the value of I'_{snc} can be extracted directly

TABLE II
BUFFER LAYER IGBT MODEL PARAMETERS (300 K)

N_L	$1.5 \times 10^{14} \text{ cm}^{-3}$
N_H	$2.4 \times 10^{17} \text{ cm}^{-3}$
W_L	60 μm
W_H	7 μm
τ_L	0.140 μs
τ_H	0.027 μs
I'_{snc}	$1.24 \times 10^{-14} \text{ A}$
A	0.035 cm^2
K_p	1.2 A/V^2
K_f	1.6
V_T	5.0 V
V_{Td}	-5.0 V
A_{gd}	0.017 cm^2
C_{oxd}	0.33 nF
C_{gs}	0.35 nF

using the tail size or decay rate described above. The on-state voltage is also influenced slightly by the value of N_H , but the most direct method of extracting N_H is through the reverse-biased emitter-base capacitance versus anode voltage. The extraction techniques for the remaining parameters in Table II are similar to those of the NB-IGBT [8], [15]. The device active area A is obtained by decapsulating the chip and measuring the area inside of the field rings at the edges of the chip. The MOSFET channel current parameters K_p , K_f , and V_T are obtained in the same way as for the NB-IGBT except that the steady-state current gain of the bipolar transistor is given by the B-IGBT expressions. Finally, the extraction procedure used to obtain the MOSFET capacitance parameters A_{gd} , C_{oxd} , and C_{gs} is identical to that for the NB-IGBT.

V. DISCUSSION AND MODEL VERIFICATION

Fig. 7 shows the measured and simulated turn-off current and voltage waveforms of (a) a B-IGBT and (b) an NB-IGBT for the clamped inductive load circuit of Fig. 4, where each curve in Fig. 7 is for a different clamp supply voltage. The model parameters for the NB-IGBT are the same as for the 0.3- μs device in [6], and the model parameters for the B-IGBT are given in Table II, with the lifetime temperature coefficients obtained from Fig. 6. To simplify the comparison between the two device types, the waveforms shown for the B-IGBT are for a temperature of 400 K and those shown for the NB-IGBT are for a temperature of 300 K. For equal temperatures, the B-IGBT switches several times faster than the NB-IGBT and a direct comparison is more difficult. The agreement between theory and experiment for the NB-IGBT's at 400 K (not shown) and the B-IGBT's at 300 K (not shown) is comparable to that shown in Fig. 7.

A. Anode Voltage Rise

The turn-off transient of Fig. 7 is initiated when the gate voltage is switched below the MOSFET channel threshold voltage ($0 < \text{time} < 20 \text{ ns}$ in Fig. 7) which removes the

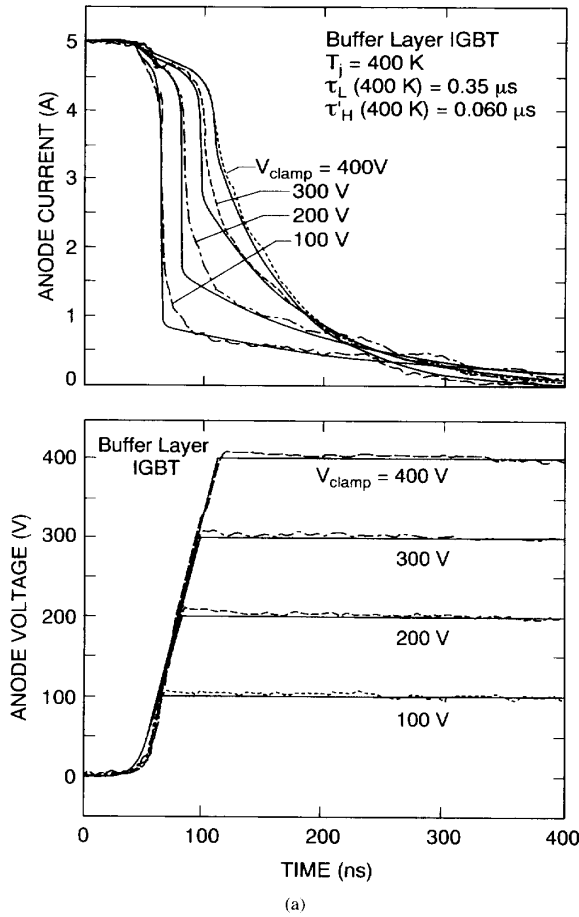


Fig. 7(a). Measured (dashed) and simulated (solid). B-IGBT anode current and anode voltage turn-off waveforms for a clamped inductive load.

MOSFET channel current. This results in a rapid anode voltage rate-of-rise that maintains a constant current in the load inductor due to the current in the IGBT effective output capacitance. The anode voltage rate-of-rise is well described by the model for both the B-IGBT and NB-IGBT waveforms in Fig. 7. The effective output capacitance is primarily determined by the moving boundary redistribution capacitance (C_{cer} in Table I) [7]. The magnitude of this capacitance depends upon the charge that is stored in the base during the steady-state condition prior to the initiation of the turn-off. The phenomena that determine the steady-state charge and the influence of the charge on the moving boundary redistribution capacitance differ between the B-IGBT and NB-IGBT.

For the B-IGBT of Fig. 7(a), the total steady-state charge that is stored in the base is reduced by approximately 30% due to the coupling between the transport of electrons and holes in the LDB. This occurs because the first term in (9) reduces the amount of LDB charge required to produce a hole current in the LDB equal to that in the HDB. Thus, the ratio of the HDB charge to the LDB charge is increased, and a smaller total steady-state base charge results for a given steady-

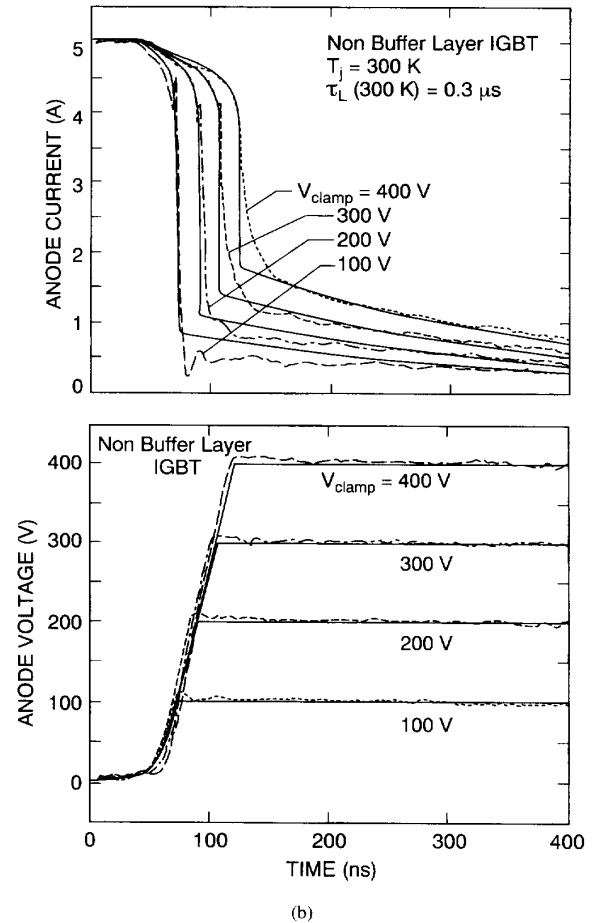


Fig. 7(b). Measured (dashed) and simulated (solid). NB-IGBT anode current and anode voltage turn-off waveforms for a clamped inductive load.

state MOSFET channel current (because the lifetime in the HDB is lower than that in the LDB). The moving boundary redistribution capacitance of the B-IGBT is also reduced as the collector-base depletion region extends into the LDB. This occurs because the redistribution capacitance is determined by the charge in the LDB, and this charge is swept into the HDB as the LDB becomes depleted. Therefore, the redistribution capacitance approaches zero and the anode voltage rate-of-rise can increase as the collector-base depletion region reaches through to the HDB.

B. Anode Current Decay

During the anode voltage rise, the anode current is reduced slightly due to the displacement current in the reverse-biased clamp diode capacitance. After the anode voltage reaches the clamp voltage, the anode voltage remains constant at the clamp voltage, and the IGBT anode current decays in two phases. 1) The anode current initially falls rapidly due to the removal of the current through the IGBT output capacitance and the removal of the associated component of hole current due to the coupling between the transport of electrons and holes for ambipolar transport. 2) This rapid fall in current is

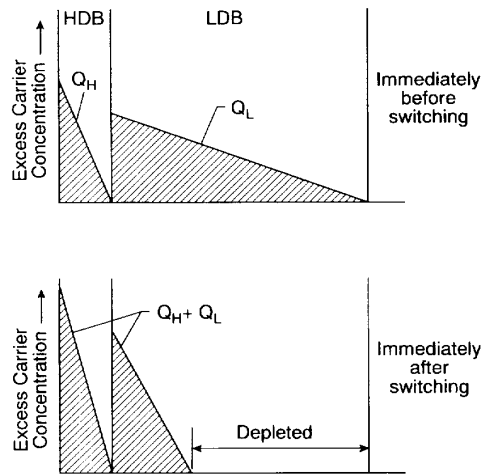


Fig. 8. Schematic of the carrier distribution in the HDB and LDB before and during turn-off of the B-IGBT.

followed by an anode current tail with a slower decay rate due to the remaining excess carriers in the base that decay by recombination in the HDB and LDB and by injection of electrons into the emitter.

Figure 8 is a schematic of the carrier distribution in the HDB and LDB before and during turn-off of the B-IGBT. As the anode voltage rises, the excess carriers are swept into the HDB and a narrower LDB because the LDB becomes depleted. For higher clamp voltages, the initial value of the tail current is larger because the quasineutral LDB is narrower and the slope of the excess carrier distribution is larger. At low clamp voltages, the initial tail size increases slightly more with increased clamp voltage for the B-IGBT of Fig. 7(a) than for the NB-IGBT of Fig. 7(b) because the LDB is narrower and the LDB dopant density is smaller for the B-IGBT device used in this example. However, the initial tail size of the B-IGBT does not continue to increase for clamp voltages larger than the reach-through voltage, whereas the tail size continues to increase at high clamp voltages for the NB-IGBT.

The charge decay rate also becomes faster at high clamp voltages for the B-IGBT, because more of the charge is in the HDB which has a lower lifetime than the LDB. The effective lifetime of the B-IGBT at $V_{clamp} = 100$ V and a temperature of 400 K is approximately equal to the $0.3\text{-}\mu\text{s}$ base lifetime of the NB-IGBT at the temperature of 300 K. Therefore, the current waveforms for $V_{clamp} = 100$ V are similar for the B-IGBT and NB-IGBT in Figs. 7(a) and 7(b). At higher clamp voltages though, the effective lifetime of the B-IGBT decreases with increasing clamp voltage (see Fig. 5), whereas the decay rate for the NB-IGBT is equal to the LDB lifetime and is independent of clamp voltage. Because the B-IGBT tail current decay rate becomes faster at high voltages, the current waveforms for the high clamp voltages cross over the current waveforms for the low clamp voltages (see Fig. 7(a) at $time = 250$ ns). Conversely, the current waveforms of the NB-IGBT for different clamp voltages asymptotically approach zero with the same time constant and do not cross over one another (Fig. 7(b)).

C. Switching Energy Losses

As described above, the switching speed of the B-IGBT can become much faster at high anode voltages than an NB-IGBT with a similar low voltage switching speed. Therefore, the voltage-independent switching speed (or switching energy loss) specified in manufacturers' data sheets does not provide sufficient information to determine the advantages of different devices in different circuit applications. A more complete method of specifying the switching speed for IGBT's is to define the normalized switching energy as the "switching time"

$$T_{sw} \equiv \frac{E_{sw}}{V_{clamp} \cdot I_T(0^-)} \quad (49)$$

This effective turn-off switching time plotted versus clamp voltage for different temperatures can be used to determine the energy losses for different applications.

For the devices of Fig. 7, the turn-off switching time of the NB-IGBT increases more with increased clamp voltage than the B-IGBT, and the switching time of both devices is relatively independent of current. However, IGBT's with longer lifetimes or reduced emitter efficiencies typically have a significant dependence of switching time on current due to the injection of electrons into the emitter. For these devices, several T_{sw} versus clamp voltage curves at different currents are necessary to describe the bias dependence of the switching speed. In addition, IGBT's with very large base widths (e.g., $200\ \mu\text{m}$) have a longer switching time at low voltages due to the longer lifetime required to conductivity-modulate the wider base, but the switching time decreases less with increased clamp voltage because the collector-base depletion region produces a smaller relative reduction in the larger value of W . Devices produced using wafer bond technology typically require larger base widths to avoid very thin wafers.

The switching energy used in (49) is readily obtained from the simulated waveforms of Fig. 7 using the Saber PLTOOL waveform calculator to integrate the IGBT dissipated power waveform [16]. The IGBT dissipated power is calculated by the model using the internal components of current and voltage and is available in the signal list of the IGBT model. The integral of this dissipated power results in a waveform for the cumulative energy losses within the IGBT. The switching energy is then calculated by subtracting the value of cumulative energy loss after switching from the value immediately before switching. The entire calculation can be performed with a few mouse-driven operations once the switching event has been simulated. This method of calculating the switching energy losses avoids the difficulty in measuring the high-speed electrical waveforms accurately enough to calculate the losses, or the difficulty in using complicated temperature measurement methods. This procedure can also be used to determine the energy losses for user-defined application conditions and thus can be used as an aid to selecting device types that maximize circuit efficiency in a given application.

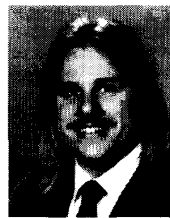
VI. CONCLUSIONS

The switching speed of IGBT's varies with bias conditions, and B-IGBT's can become faster at high voltages than NB-

IGBT's with similar switching speeds at low voltages. Therefore, the single switching speed specified in manufacturers' data sheets does not provide sufficient information for circuit designers to select the most appropriate part for a specific application. However, a new B-IGBT model has been developed that can be used to compare the behavior of different IGBT's in user-defined circuit application conditions. A B-IGBT model parameter extraction procedure has also been developed that can be used to develop IGBT component libraries for circuit simulators. Furthermore, the B-IGBT model can be used to design custom IGBT's that are optimized for a given circuit operating condition, because the breakdown voltage, on-state voltage, and the switching energy can be calculated for devices with different HDB and LDB widths and dopant densities.

REFERENCES

- [1] H. W. Becke and C. F. Wheatley, "Power MOSFET's with an anode region," United States Patent 4,364,073, 1982.
- [2] B. J. Baliga, M. S. Adler, P. V. Gray, R. P. Love, and N. Zommer, "The insulated gate rectifier: (IGR)" in *Conf. Proc. IEEE IEDM*, p. 264, 1982.
- [3] A. R. Hefner and D. L. Blackburn, "An analytical model for the steady-state and transient characteristics of the power insulated gate bipolar transistor," *Solid-State Electron.*, vol. 31, p. 1513, 1988.
- [4] ———, "Performance trade-off for the insulated gate bipolar transistor: buffer layer versus base lifetime reduction," *IEEE Trans. Power Electron.*, PE-2, p. 194, 1987; also in *IEEE PESC Conf. Rec.*, p. 27, 1986.
- [5] A. R. Hefner, "Analytical modeling of device-circuit interactions for the power insulated gate bipolar transistor (IGBT)," in *IEEE IAS Conf. Rec.*, p. 606, 1988; also in *IEEE Trans. Ind. Appl.*, IA-26, p. 995, 1990.
- [6] ———, "An investigation of the drive circuit requirements for the power insulated gate bipolar transistor (IGBT)," in *IEEE PESC Conf. Rec.*, p. 126, 1990; also in *IEEE Trans. Power Electron.*, PE-6, p. 208, 1991.
- [7] ———, "An improved understanding for the transient operation of the power insulated gate bipolar transistor (IGBT)," in *IEEE PESC Conf. Rec.*, p. 303, 1989; also in *IEEE Trans. Power Electron.*, PE-5, p. 459, 1990.
- [8] ———, "Semiconductor measurement technology: INSTANT - IGBT network simulation and transient analysis tool," NIST Special Publication 400-88, 1992.
- [9] A. R. Hefner and D. M. Diebolt, "An experimentally verified IGBT model implemented in the saber circuit simulator," in *IEEE PESC Conf. Rec.*, p. 10, 1991; also in *IEEE Trans. Power Electron.*, vol. 9, 1994.
- [10] C. S. Mitter, A. R. Hefner, D. Y. Chen, and F. C. Lee, "Insulated gate bipolar transistor (IGBT) modeling using IG-SPICE," in *IEEE IAS Conf. Rec.*, p. 1515, 1991; also in *IEEE Trans. Ind. Applicat.*, IA-30, 24, 1994.
- [11] A. R. Hefner, "A dynamic electro-thermal model for the IGBT," in *IEEE IAS Conf. Rec.*, p. 1094, 1992; also in *IEEE Trans. Ind. Applicat.*, vol. 30, p. 394, 1994.
- [12] A. R. Hefner and D. L. Blackburn, "Simulating the dynamic electro-thermal behavior of power electronic circuits and systems," in *Conf. Rec. IEEE Workshop on Computers in Power Electronics*, p. 143 (1992); also in *IEEE Transactions on Power Electronics*, vol. 8, pp. 376 (1993).
- [13] ———, "Thermal component models for electro-thermal network simulation," in *Proc. IEEE Semiconductor Thermal Measurement and Manage. SEMI-THERM Symp.*, p. 88, 1993; also in *IEEE Trans. Components, Packaging, and Manufacturing Technol.*, vol. 17, p. 413, 1994.
- [14] S. Selberherr, *Analysis and Simulation of Semiconductor Devices*. New York: Springer-Verlag, 1984, p. 88.
- [15] A. R. Hefner, "Device models, circuit simulation, and computer-controlled measurements for the IGBT," in *Conf. Rec. IEEE Workshop Computers in Power Electron.*, p. 233, 1990.
- [16] H. A. Mantooth and A. R. Hefner, "Electro-thermal simulation of an IGBT PWM inverter," in *IEEE PESC Conf. Rec.*, 1993.



Allen R. Hefner, Jr. (S'84-M'84-SM'93) was born in Washington, DC, on June 29, 1959. He received the B.S., M.S., and Ph.D. degrees in electrical engineering from the University of Maryland in 1983, 1985, and 1987, respectively.

He joined the Semiconductor Electronics Division of the National Institute of Standards and Technology (formerly the National Bureau of Standards) in 1983. He is currently Project Leader for the Electrical and Thermal Characterization Project in the Device Technology Group of the Semiconductor

Division at NIST. His research interests include characterization, modeling, and circuit utilization of power semiconductor devices. He is the author of 20 publications in IEEE TRANSACTIONS and conference proceedings.

Dr. Hefner received the U.S. Department of Commerce Silver Medal Award for his pioneering work in modeling advanced power semiconductor devices for electro-thermal circuit simulation. He is also the recipient of an IEEE Industry Applications Society prize paper award. He was an instructor for the IEEE Power Electronics Specialist Conference tutorial course in 1991 and 1993 and for the IEEE Industry Applications Society Meeting tutorial course in 1994. He has served as a program committee member for the IEEE Power Electronics Specialist Conference in 1991-95 and as the IEEE Industry Applications Society TRANSACTIONS Review Chairman for the Power Electronics Devices and Components Committee in 1989-1994.